Phonons and the lattice dynamics in crystals with atomic diffusion: Concept and application to superionic ices

Hairui Ding [1], Artem R. Oganov [2], Haixu Cui,[3] Jiachang Zhang,[1] and Xiao Dong [1,*]
[1]*Key Laboratory of Weak-Light Nonlinear Photonics, School of Physics, Nankai University, Tianjin 300071, China*
[2]*Skolkovo Institute of Science and Technology, Moscow 121205, Russia*
[3]*College of Physics and Materials Science, Tianjin Normal University, Tianjin 300387, China*

(Received 19 August 2025; revised 14 February 2026; accepted 11 June 2026; published 1 July 2026)

Phonons, the quantized collective excitations of crystal lattice vibrations, require long-range periodic order for momentum to be a well-defined quantum number—a condition that breaks down in disordered systems. However, many systems exhibit a complex interplay between ordered and disordered components. A prime example is superionic ice, a novel phase of ice at high temperatures and pressures, where hydrogen ions (protons) diffuse like a liquid while oxygen ions maintain a solidlike vibrational framework. Previous research has mainly focused on the diffusive aspect of the superionic phase, leaving the rich physics of its vibrational lattice dynamics relatively unexplored. Here, we investigate the phonon properties of superionic ices with both body-centered-cubic (bcc) and face-centered-cubic (fcc) oxygen sublattice. Despite the fully disordered protons, the oxygen sublattice exhibits similar phonon dispersion with typical bcc/fcc solids. This similarity is not a trivial regression, but direct evidence of the emergence of higher symmetry and effective interaction degeneracy resulting from hydrogen-bond dissociation, accompanied by strong damping and anharmonicity. Notably, we identify that specific softened phonon modes drive the mechanical instability of the bcc oxygen sublattice, providing a key kinetic mechanism for phase transitions between superionic ices. By extending the phonon concept to a hybrid ordered-disordered system, our work provides a powerful framework for characterizing lattice dynamics in superionic and related complex materials.

DOI: 10.1103/m1s6-6hdf

I. INTRODUCTION

Water molecules, though simple, exhibit a rich variety of phases governed by hydrogen bonding. Hydrogen bonds in ice are usually formed by O···H-O pairs, characterized by a double-well potential symmetric about the midpoint between two oxygen ions. Hydrogen ion (proton) occupies one of two wells, as seen in ambient ice Ih and high-pressure ice VII (stable at ∼2–50 GPa) [1]. With pressure increasing, the O-O distances decrease, causing the two potential wells to converge and merge. This process culminates in the formation of ice X, a high-pressure phase with symmetric hydrogen bonds [2–6], as shown in Fig. 1(d). Further increases in both pressure and temperature lead to the emergence of a new superionic phase. Specifically, superionic ice retains oxygen sublattice with long-range order, while protons diffuse like liquid within it [7–11]. As one of the most common substances in the universe, high-pressure ice is crucial for understanding planetary science as well as fundamental physics and chemistry at extreme conditions.

Superionic ice uniquely combines properties of solid ice and liquid water, occupying an intermediate region between the solid and liquid phases in the pressure-temperature (P-T) phase diagram, as shown in Fig. 1(a). The phase boundaries demarcating the superionic ice from solid ice and from liquid water have been extensively investigated in both experiments and computations [11–16]. Superionic ice begins to appear at pressures above ∼30 GPa. With increasing pressure, the proton melting temperature (defining the solid-to-superionic transition) grows more slowly than the oxygen sublattice melting temperature (defining the superionic-to-liquid transition). The region of stability of superionic ice is bounded by the two melting curves.

Within this region, two primary types of superionic ice are proposed, one with body-centered-cubic (bcc) oxygen sublattice and another with face-centered-cubic (fcc) oxygen sublattice, shown in Figs. 1(b) and 1(c). Both are expected to be dominant constituents in the mantles of ice giant planets. Although the precise stability domains of these phases vary somewhat among previous investigations [11–16] and the present work, the overall trends remain consistent: bcc superionic ice is favored at lower pressures and temperatures, whereas fcc superionic ice is stable at higher pressures and temperatures. Furthermore, despite the fact that solid ice X and bcc superionic ice share the same bcc oxygen sublattice, ice X is stable at very high pressures, while bcc superionic ice only occupies a small region below ∼100 GPa. Notably, various phase diagrams display a direct boundary between ice X and fcc superionic ice, without an intervening bcc superionic transition phase. Although these phase diagrams rationalize such observations on the basis of free-energy considerations, the underlying mechanism of the phase transition, particularly with respect to its manifestation in lattice dynamics, remains unclear.

Compared with solid ice, superionic ices lack well-defined hydrogen-bond networks, having instead dynamic and

*Contact author: xiao.dong@nankai.edu.cn

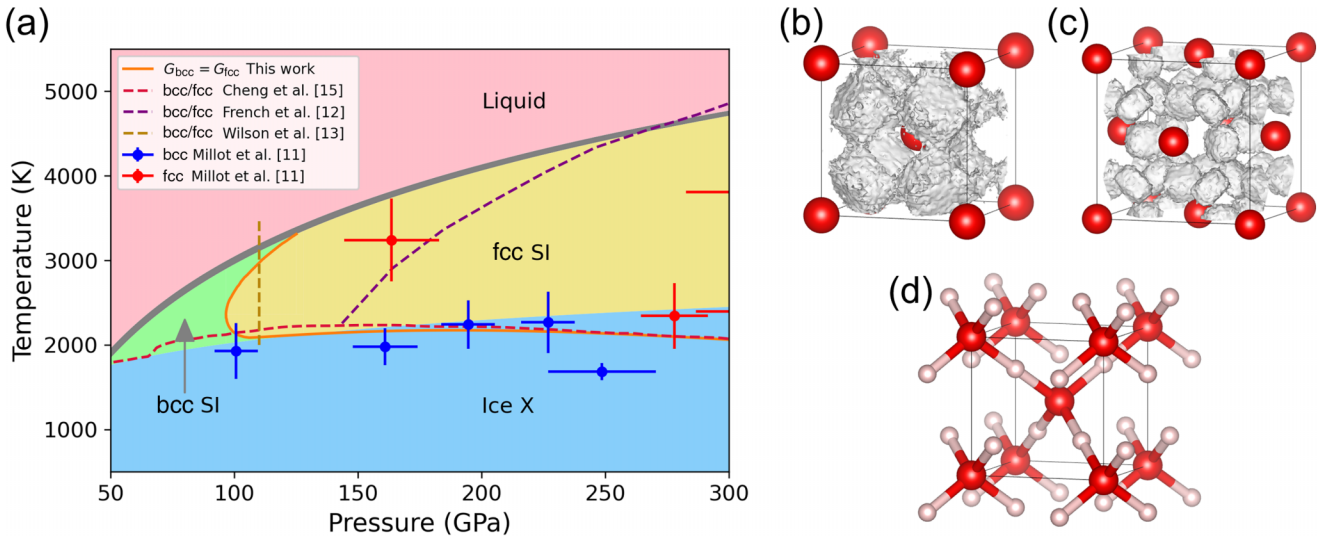

FIG. 1. (a) Phase diagram of high-pressure ices, and atomic structures of (b) bcc, (c) fcc superionic ices (SI), and (d) ice X. In panel (a), the upper and lower boundaries of the thick gray curve correspond to the oxygen melting curves of bcc and fcc superionic ice, respectively. The solid orange curve is our calculated phase boundary of bcc and fcc ices, with dashed curves from other studies. Oxygen atoms are red spheres in (b)–(d). Hydrogen atoms in ice X are shown as small pink spheres. In superionic ices, white isosurfaces indicate the probability density distribution of mobile hydrogen ions (protons).

disordered H-O interactions. Superionic ice can be viewed as a crystal formed by oxygen ions immersed in a sea of protons (quite similar to the usual depiction of metals as crystals formed by ionic cores immersed in electron gas). Dissociation of hydrogen bonds reduces the shear resistance of superionic ice, as demonstrated in previous studies [17,18], and again in close analogy with typical metals having low shear moduli. Nevertheless, the change in elastic properties is only one manifestation of phase transition mechanisms. A comprehensive understanding of vibrational behavior necessitates phonon analysis for both normal and superionic ices. However, compared even to disordered nonsuperionic phases such as ice VII, the protons in superionic ice exhibit vastly greater mobility and disorder, resulting in an extensive configurational space and the failure of harmonic/quasiharmonic approximation.

In this paper, we address this gap by combining machine-learning potential (MLP) with spectral energy density (SED) analysis, enabling the detailed phonon characterization across solid ice X and both bcc and fcc superionic ices over wide pressure and temperature ranges. We uncover a strikingly simple picture: upon hydrogen-bond dissociation, the oxygen sublattice evolves into a higher-symmetry framework, which can be described by a set of effective Born–von Kármán force constants. This indicates that the vibrations of superionic phases still fall within the scope of lattice dynamics, with disordered protons acting as a mean field. Critically, a specific transverse acoustic mode softens upon superionization, and drives the bcc-to-fcc superionic phase transition, which directly explains the narrow stability of bcc superionic ice and the observed direct ice X-fcc phase boundary. Moreover, mobile protons bring strong anharmonicity and phonon damping, implying decreasing lattice thermal conductivity in superionic ice [19].

II. METHODS

A. Phonon calculation

Conventional lattice dynamics, based on the quasiharmonic approximation, calculates phonon dispersions by assuming atoms vibrate within local potential wells. This approach fails for superionic systems where ionic diffusion causes force constants to dynamically fluctuate. Displaced to a very large extent, diffusing atoms sample extremely anharmonic parts of the energy surface, invalidating the traditional harmonic and quasiharmonic approaches. Instead, we compute phonon properties directly from atomic trajectories via SED analysis [20]. The SED spectrum fully characterizes phonon dispersions and lifetimes by quantifying the kinetic-energy distribution across reciprocal space and frequency domains, capturing both vibrational and diffusive components. By projecting SED onto atomic subsets, we separate the vibrational spectrum of the oxygen sublattice from diffusive protons in superionic ice. This method inherently accounts for dynamic H-O interactions in all studied phases. With the same idea, phonon density of states (DOS) is obtained from the Fourier transform of atomic velocity autocorrelation functions (detailed in the Supplemental Material [21]).

B. Machine-learning potential

In this study, molecular dynamics (MD) trajectories were simulated using the neuroevolution potential (NEP) [22]. To ensure accuracy and capture long-range interactions critical for phonon analysis in superionic ice, we trained a NEP on *ab initio* MD data (implemented in VASP [23]) from small systems (see Fig. S4 in the Supplemental Material [21] for the training result), then performed simulations with more than 3.5×10^5 atoms. This large-scale approach overcomes

TABLE I. Densities, sound velocities, and elastic constants of the oxygen sublattices in bcc and fcc superionic ices at 3000 K, 200 GPa. Values in parentheses are from Ref. [17], where the bcc superionic ice is simulated at 2000 K, 200 GPa, and the fcc one is at 3000 K, 200 GPa.

Properties	bcc	fcc
ρ (g/cm^3)	3.80 (3.65)	3.79 (3.61)
$v_{L[110]}$ (km/s)	17.19 ± 0.53	17.00 ± 0.51
$v_{T1[110]}$ (km/s)	9.95 ± 0.47	9.47 ± 0.55
$v_{T2[110]}$ (km/s)	2.89 ± 0.64	3.83 ± 0.54
C_{11} (GPa)	777.11 ± 61.11 (794.9)	816.13 ± 54.88 (759.1)
C_{12} (GPa)	711.98 ± 57.78 (685.0)	703.92 ± 50.20 (640.0)
C_{44} (GPa)	377.21 ± 35.57 (430.0)	338.52 ± 39.52 (288.7)

size effects known to compromise SED resolution [24], as illustrated in Fig. S10 in the Supplemental Material [21], particularly where phonon scattering and proton dynamics dominate. More details about training and validation of the NEP are listed in the Supplemental Material [21].

C. Phase diagram calculation

In our calculated phase diagram shown in Fig. 1(a), the phase boundary between bcc and fcc superionic ices is determined by free-energy calculation, and the superionization curve and oxygen melting curve are determined by the two-phase method (see Fig. S12 in the Supplemental Material [21]). These calculations are detailed in the Supplemental Material [21].

D. Elastic properties calculation

The group velocities of acoustic phonon branches near the Γ point (linear long-wavelength region) are velocities of sound waves with corresponding modes. Based on the Christoffel equation [25], the elastic constants can be derived from sound velocities. For a cubic lattice, the elastic constants can be obtained by sound velocities of three modes propagating along the [110] direction, in principle. In Table I, the listed elastic constants are obtained by averaging over all modes propagating along the [110], [001], and [111] directions. The results calculated by the two methods are identical within 0.5%.

III. RESULTS AND DISCUSSION

A. Phonon dispersion of bcc superionic ice

We first calculate the phonon SED of solid ice X to validate our methodology and trained MLP, as shown in Fig. S1 in the Supplemental Material [21]. The calculated phonon dispersion is in good agreement with previous study [26] and that calculated by the finite-displacement method (implemented by PHONOPY [27]; see Fig. S11 in the Supplemental Material [21]), confirming the reliability of the MLP. Projected phonon DOS in Fig. S1 in the Supplemental Material [21] reveals that high-frequency vibrations are predominantly associated with hydrogen ions, with the peak near 100 THz corresponding to the H-O stretching mode [9].

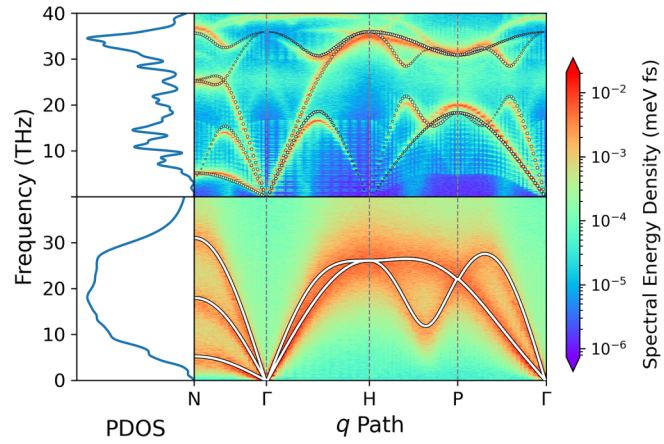

FIG. 2. Phonon DOS (left) and SED (right) of solid ice X at 500 K (top) and bcc superionic ice at 3000 K (bottom) and 200 GPa. The $\boldsymbol{q}$ path is generated along the high-symmetry reciprocal path of a bcc lattice. Open circles in the top panel and white curves in the bottom panel are fitted phonon dispersions by lattice dynamics. Sizes of the circles are proportional to the unfolding weights of the corresponding phonon modes. The fitted force constants are listed in Table S1 in the Supplemental Material [21].

As ice X undergoes a phase transition to the bcc superionic ice, its symmetric hydrogen bonds dissociate and hydrogen ions display a diffusive liquidlike dynamics, with a continuous frequency spectrum in DOS. Crucially, the nonzero hydrogen DOS at zero frequency provides direct evidence of proton diffusivity (see Fig. S1 in the Supplemental Material [21]). Scattered by diffusive protons, phonon modes of the oxygen sublattice exhibit increased linewidths (broader peaks) and a smoother DOS profile. Nevertheless, as Fig. S1 in the Supplemental Material [21] demonstrates, the phonon modes of the oxygen sublattice retain well-defined momentum ($\boldsymbol{q}$ vector) in the low-frequency region. In contrast, the highly mobile protons, lacking long-range order, are absent from the SED spectrum. This indicates that the concept of phonons is ill defined for the diffusive protons. Consequently, the hydrogen vibrational spectrum appears as a homogeneous background of SED. Therefore, subsequent analysis focuses solely on the phonon properties of the oxygen sublattice.

For clarity, phonon SEDs are projected to an oxygen sublattice, and zoomed in to the low-frequency range as displayed in Fig. 2. Even though oxygen ions occupy the same positions within the cubic cells of ice X and bcc superionic ice (and can be described as a body-centered-cubic sublattice), their dynamical behavior is different. In bcc superionic ice, each oxygen ion has eight equivalent interactions with the nearest oxygen ions. In ice X, however, due to the localization of hydrogens at the midpoints of four of these O-O vectors, and the absence of hydrogen atoms on the other four O-O vectors (see Fig. S2 in the Supplemental Material [21]), asymmetry is introduced between the two sets of O-O interactions despite the same O-O distance. Ice X has the same peculiar crystal structure as mineral cuprite (Cu_2O), a three-dimensional (3D)-catenane made of two interpenetrating (but never intersecting) tetrahedral frameworks; this has also been described as a double-diamond structure [28]. This model, originally

proposed to describe the asymmetric O-O interactions in ice VII and inherited by ice X, involves two interpenetrating diamondlike oxygen sublattices. Crucially, while this model predicts the absence of a gap at the P point ($\boldsymbol{q} = \frac{1}{2}[111]$) for structures such as ice VII and bcc superionic ice (attributed to hydrogen disorder), it fails to account for the pronounced gap clearly observed at the P point in our phonon spectrum of ice X (see Fig. S5 in the Supplemental Material [21]), consistent with quasiharmonic results [26].

To resolve this discrepancy for ice X, we proposed a different asymmetry parameter that modifies the O-O elastic interaction within the lattice (see the Supplemental Material [21]), which yields excellent agreement with the SED of ice X (Fig. 2). We note that our large-scale calculation for ice VII (see Fig. S6 in the Supplemental Material [21]) also reveals a small, blurred gap (∼3.61 THz) at the P point, contrasting with the sharp ∼11.69 THz gap in ice X and its complete absence in bcc superionic ice. The gap at the P point originates from the symmetry-breaking distinction between two sets of nearest-neighbor O-O interactions within the bcc oxygen sublattice, induced by hydrogen-bond ordering of ice X. In bcc superionic ice, fully disordered protons render these two sets of O-O interactions identical, restoring the full symmetry of the bcc lattice and eliminating the gap at the P point. While ensemble averaging over proton configurations in ice VII suggests a similar restoration of bcc symmetry—where hydrogen bonds are effectively averaged across all possible O-O pairs—this leads to gap closure at the P point, as observed in Ref. [28] and analogous to superionic ice. However, hydrogen disorder in ice VII differs fundamentally: the topology of its hydrogen-bond networks remains fixed during molecular dynamics simulations. Protons neither dissociate from existing O-H···O bonds nor form new hydrogen bonds with previously unconnected O-O pairs. Consequently, the intrinsic asymmetry between the two sets of O-O interactions persists. Our SED calculations capture this persistent structural asymmetry, revealing the gap at the P point.

B. Soft phonon modes and phase transitions for bcc superionic ice

In superionic ice, protons diffuse through the oxygen framework, causing instantaneous H-O interactions to fluctuate rapidly. On average, the symmetry of superionic bcc ice ($Im3m$) is higher than that of ice X ($Pn3m$); consequently, phonon modes of the oxygen sublattice in bcc superionic ice exhibit degeneracies at multiple $\boldsymbol{q}$ points, signifying that the double-diamond structure of ice X has evolved into a higher-symmetry bcc arrangement. The resulting phonon dispersion closely resembles that of typical bcc crystals and is well described by a simple Born–von Kármán model considering interactions up to the second-nearest neighbors (detailed in the Supplemental Material [21]). The symmetry-breaking effect of localized hydrogen bonds present in ice X vanishes in the superionic state, leading to the closure of phonon gaps. Meanwhile, hydrogen-bond dissociation weakens the effective interactions between oxygen ions, reflected in reduced values of the interatomic force constants (see Table S1 in the Supplemental Material [21]).

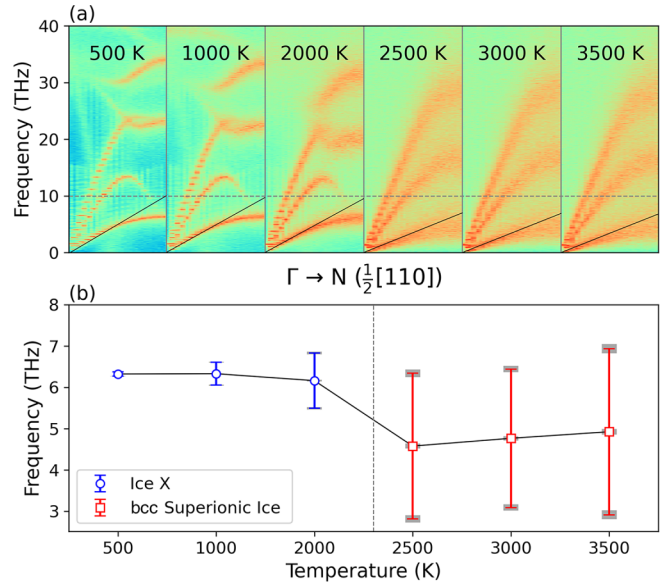

FIG. 3. (a) Phonon branches along the [110] direction ($\boldsymbol{q}$ path from the Γ to N point) vary with temperature in bcc ice at 200 GPa. Black solid lines are linear fits to the long-wavelength regions of the $T_{[1\bar{1}0]}[110]$ phonon modes. Gray dashed line indicates the location of frequency at 10 THz. (b) Temperature dependency of center frequency and linewidth of the $T_{[1\bar{1}0]}[110]$ mode at the N point, where the gray dashed vertical line indicates the approximate superionization temperature (∼2300 K at 200 GPa), and the uncertainties of these data are represented by shaded regions.

Phonon SED also provides crucial information about phonon lifetimes, which is a key aspect of lattice dynamic analysis. The validity of the phonon concept itself hinges on its lifetime exceeding its vibrational period. At each wave vector $\boldsymbol{q}_0$, the frequency spread of each mode with center frequency ω_c follows the Lorentzian function [20]: $\mathrm{SED}(\boldsymbol{q}_0,\ \omega) \propto \frac{1}{1+[(\omega-\omega_c)/\gamma]^2}$, and phonon lifetime τ being defined as inverse of the linewidth or the full width at half maximum (FWHM) of the peak 2γ: $\tau = \frac{1}{2\gamma}$. In superionic ice, phonons experience frequent scattering by diffusive protons. This leads to drastically shortened mean free paths and lifetimes, manifest as broadened branches in the SED. In particular, the transverse acoustic branch along the Γ-N path ([110] direction) with $[1\bar{1}0]$ polarization, denoted as $T_{[1\bar{1}0]}[110]$ modes, exhibits frequencies below or near 5 THz. As shown in Fig. 3, the linewidths of these modes can reach up to 4.88 THz (corresponding to the lifetime ∼0.20 ps). For the mode with comparable center frequency and linewidth, i.e., comparable lifetime and vibration time period, the phonon is strongly damped and would extinguish. This signifies a substantial probability for the mode to soften to zero frequency, marking the inability of the structure to resist certain displacements of the atoms. Figure 3(b) illustrate this for the $T_{[1\bar{1}0]}[110]$ modes specifically at the N point ($\boldsymbol{q} = \frac{1}{2}[110]$), which shows a dramatic increase in linewidth upon entering the superionic phase. On the one hand, large broadening or short lifetime significantly reduces thermal transport efficiency due to phonons, consistent with reported calculations where lattice thermal conductivity of superionic ice was found

to be lower than that of solid ice [19,29]. On the other hand, large linewidth promotes lattice instability, increasing the likelihood of mode extinction and potentially triggering an irreversible phase transition. Therefore, dynamic SED analysis serves as a vital complement to static quasiharmonic phonon theory, particularly for understanding phase transitions driven by soft modes. Our findings indicate that this phonon softening mechanism drives phase transitions in superionic ice.

The $T_{[1\bar{1}0]}[110]$ modes in the bcc lattice are responsible for two phase transitions of bcc to both hexagonal-close-packed (hcp) and fcc structures [30]. As depicted in Fig. S3 in the Supplemental Material [21], the (110) planes of the bcc lattice have an ABAB … stacking sequence. The $T_{[1\bar{1}0]}[110]$ modes involve vibrations of these planes along the $[1\bar{1}0]$ direction. At short wavelength, especially $\boldsymbol{q} = \frac{1}{2}[110]$ that is equal to double interplanar spacing of (110) planes, the ABAB … stacking is able to persist. Meanwhile, with the assistance of long-wavelength $T_{[1\bar{1}2]}[\bar{1}11]$ modes, which shears the hexagonal arrangement on (110) planes into regular hexagonal, the bcc lattice can be finally transform to the hcp structure. Some previous studies [13–14] suggest that hcp and fcc superionic ices can coexist and interconvert, having very similar energies (as is usual for polytypes, the energy differences of which are often not easy to distinguish). However, it was reported that fcc superionic ice has a slightly lower Gibbs free energy at pressures below 400 GPa [15], which implies that the main approach for the phase transitions of bcc superionic ice is bcc-to-fcc, rather than bcc-to-hcp. Given this, our subsequent analysis focuses primarily on the bcc-to-fcc transition dynamics.

The long-wavelength $T_{[1\bar{1}0]}[110]$ modes, which are usually regarded as shears on lattice and characterized by the initial slope of the branch near the Γ point, soften abruptly upon hydrogen-bond dissociation, as shown in Fig. 3(a). The long-wavelength shear breaks the original ABAB … stacking sequence of the (110) planes and leads to new ABCABC … stacking. Together with $T_{[1\bar{1}2]}[\bar{1}11]$ modes, these planes are squeezed into a regular hexagonal arrangement, completing the transition to the fcc structure [30]. Overall, the unstable $T_{[1\bar{1}0]}[110]$ modes correspond to the slipping between (110) planes. In solid ice X, hydrogen bonds bridging neighboring (110) planes resist compression and stretch, effectively hindering such slip. This explains the relative stability of the long-wavelength $T_{[1\bar{1}0]}[110]$ shear in ice X and its abrupt decrease upon superionization. The temperature dependence indicates the trend of the oxygen sublattice to transform from a bcc to fcc structure, which can also be seen at other pressures (see Fig. S13 in the Supplemental Material [21]), rationalizing the fact that the bcc-fcc phase boundary is close to the superionization curve at high pressures in the phase diagram [11,14–16].

Another soft longitudinal mode lies near 2/3 of the [111] direction, denoted as $L\frac{2}{3}[111]$. This mode has been widely studied for the bcc-ω phase transition [31]. The (111) planes in the bcc structure have an ABCABC … stacking sequence. In the $L\frac{2}{3}[111]$ mode, one plane is fixed and the other two neighboring planes move towards each other along the [111] direction and merge into one single plane. In superionic ice, such bcc-ω transition goes a little further: the two moving planes pass through each other and exchange their positions, i.e., they become ACBACB … stacking (see the illustration in Fig. S7 in the Supplemental Material [21]; this transition is also detectable via the mean-square displacement of the oxygen sublattice, as shown in Fig. S8 in the Supplemental Material [21]). The result is a transition between two differently oriented bcc structures, indicating that the ω phase itself is unstable for the oxygen sublattice in superionic ice.

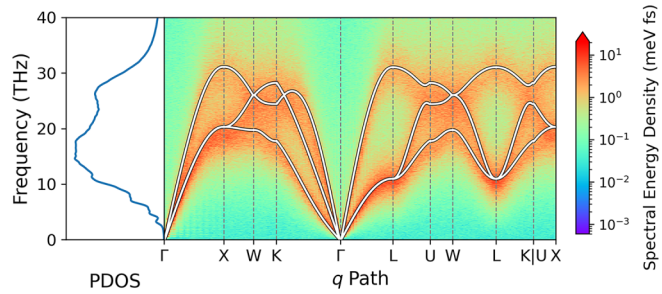

FIG. 4. Phonon DOS (left) and SED (right) of fcc superionic ice at 3000 K, 200 GPa. White curves are fitted phonon dispersion by lattice dynamics. The fitted force constants are listed in Table S1 in the Supplemental Material [21].

However, the bcc-via ω-bcc transition associated with the $L\frac{2}{3}[111]$ mode usually manifests prominently only in a small simulation cell ($3 \times 3 \times 3$) and could be suppressed by the long-range interactions in larger supercells, such as $6 \times 6 \times 6$ and larger. As shown in Fig. 2, the center frequency of this mode (11.76 THz) significantly exceeds its linewidth (5.61 THz), which indicates there is sufficient stability for the bcc lattice to avoid this transition mode. In contrast, the bcc-to-fcc transition associated with the long-wavelength $T_{[1\bar{1}0]}[110]$ mode, despite its lower frequency, cannot be directly observed in our MD simulations. This absence can be attributed to two primary factors. First, the periodic boundary conditions inherently restrict uniform shear deformations of the simulation cell, which is precisely what the $\boldsymbol{q} \to 0$ transverse mode describes. Second, the characteristic wavelength of this mode is effectively infinite compared to the finite simulation size, making its activation improbable even with large nanometer-scale models. Conversely, the collective atomic displacements involved in the $L\frac{2}{3}[111]$ mode do not require lattice deformation. In this case, a small simulation cell can be beneficial, as it naturally shortens the correlation length needed for the collective atomic motion, thereby facilitating the observation of the phase transition.

C. Phonon dispersion of fcc superionic ice

The phonon SED of fcc superionic ice is also calculated and presented in Fig. 4. Unlike the bcc phase, the fcc oxygen sublattice exhibits no distinct soft modes. The modes with the lowest frequency are two transverse modes at the Γ-L path ([111] direction), corresponding to the shears of the (111) planes. According to the Nishiyama-Wassermann orientation relationship [32], this could be a possible way for the fcc-to-bcc transition, and completely reverse to the bcc-to-fcc transition shown in Fig. S3 in the Supplemental Material [21]. However, the frequency of the two modes is much higher than the $T_{[1\bar{1}0]}[110]$ modes in bcc superionic ice, indicating

enhanced structural stability of the fcc oxygen sublattice in superionic ices.

In order to further investigate the structure stability of both sublattices, we calculate their elastic constants through dispersion relations. The results are listed in Table I and compared with previous studies by the finite strain method [17]. The slight differences come from the errors of our trained machine-learning potential, which lead to overestimated densities and biased group velocities, as well as the errors when fitting the phonon dispersion. Nevertheless, the results still align closely with previous studies [6,17], which validates the accuracy of our SED spectrum. As discussed above, the long-wavelength $T_{[1\bar{1}0]}[110]$ shear $(C_{11} - C_{12})/2$ in bcc superionic ice has a very low modulus of 31.74 GPa, corresponding to a transverse sound velocity of 2.89 km/s, indicating a near instability. In contrast, the same shear in fcc is obviously stronger with a minimum sound velocity of 3.83 km/s, which is 1.3 times that of bcc superionic ice. The phonon dispersion is also able to study the sound velocities of all directions. Figure S9 in the Supplemental Material [21] shows the SED of certain cross sections of the first Brillouin zone, where the SED slices at low frequency represent the anisotropy of sound velocities.

IV. CONCLUSIONS

Our phonon DOS and SED analyses uncover the dynamics of normal ice X and superionic bcc and fcc ices, elucidating the phase transition mechanism between the two superionic ices. Our lattice dynamics model considering the hydrogen-bond ordering of ice X explains the origin of the gaps, especially at $\boldsymbol{q} = \frac{1}{2}[111]$, distinguishing it from hydrogen-disordered ice VII. Upon hydrogen-bond dissociation at elevated temperature, the structure gains higher symmetry, and its dispersion relation degenerates to that of a typical bcc lattice; the same applies to the fcc superionic ice. Hydrogen-bond dissociation facilitates interplanar slipping within the oxygen sublattice, driving significant phonon softening. Particularly, the shear mode dominating the bcc to fcc phase transition shows pronounced softening upon superionization, explaining the low dynamical stability of bcc superionic ice. Our work extends the fundamental concept of the phonon from ordered crystals to partially disordered systems, and shows the potential of lattice dynamics analysis in hybrid ordered-disordered states, such as the superionic state, plastic state [33,34], or systems with short-range disorder and long-range order [35].

ACKNOWLEDGMENTS

The calculations were performed and supported by Tianhe II in Guangzhou. This work was supported by the National Natural Science Foundation of China (Grants No. 12574019, No. 92263101, and No. 12174200). A.R.O. thanks the Russian Science Foundation (Grant No. 19-72-30043) for support.

DATA AVAILABILITY

The scripts to calculate SED and the trained NEP files are available at GitHub [36].

[1] J. A. Hernandez and R. Caracas, Proton dynamics and the phase diagram of dense water ice, J. Chem. Phys. **148**, 214501 (2018).

[2] K. Aoki, H. Yamawaki, M. Sakashita, and H. Fujihisa, Infrared absorption study of the hydrogen-bond symmetrization in ice to 110 GPa, Phys. Rev. B **54**, 15673 (1996).

[3] A. F. Goncharov, V. V. Struzhkin, M. S. Somayazulu, R. J. Hemley, and H.-K. Mao, Compression of ice to 210 gigapascals: Infrared evidence for a symmetric hydrogen-bonded phase, Science **273**, 218 (1996).

[4] M. Benoit, D. Marx, and M. Parrinello, Tunnelling and zero-point motion in high-pressure ice, Nature (London) **392**, 258 (1998).

[5] A. F. Goncharov, V. V. Struzhkin, H.-K. Mao, and R. J. Hemley, Raman spectroscopy of dense H_2O and the transition to symmetric hydrogen bonds, Phys. Rev. Lett. **83**, 1998 (1999).

[6] J. A. Hernandez and R. Caracas, Superionic-superionic phase transitions in body-centered cubic H_2O ice, Phys. Rev. Lett. **117**, 135503 (2016).

[7] P. Demontis, R. LeSar, and M. L. Klein, New high-pressure phases of ice, Phys. Rev. Lett. **60**, 2284 (1988).

[8] C. Cavazzoni, G. L. Chiarotti, S. Scandolo, E. Tosatti, M. Bernasconi, and M. Parrinello, Superionic and metallic states of water and ammonia at giant planet conditions, Science **283**, 44 (1999).

[9] N. Goldman, L. E. Fried, I. F. W. Kuo, and C. J. Mundy, Bonding in the superionic phase of water, Phys. Rev. Lett. **94**, 217801 (2005).

[10] A. F. Goncharov, N. Goldman, L. E. Fried, J. C. Crowhurst, I. F. W. Kuo, C. J. Mundy, and J. M. Zaug, Dynamic ionization of water under extreme conditions, Phys. Rev. Lett. **94**, 125508 (2005).

[11] M. Millot, F. Coppari, J. R. Rygg, A. C. Barrios, S. Hamel, D. C. Swift, and J. H. Eggert, Nanosecond X-ray diffraction of shock-compressed superionic water ice, Nature (London) **569**, 251 (2019).

[12] M. French, M. P. Desjarlais, and R. Redmer, *Ab initio* calculation of thermodynamic potentials and entropies for superionic water, Phys. Rev. E **93**, 022140 (2016).

[13] H. F. Wilson, M. L. Wong, and B. Militzer, Superionic to superionic phase change in water: Consequences for the interiors of uranus and neptune, Phys. Rev. Lett. **110**, 151102 (2013).

[14] J. Sun, B. K. Clark, S. Torquato, and R. Car, The phase diagram of high-pressure superionic ice, Nat. Commun. **6**, 8156 (2015).

[15] B. Cheng, M. Bethkenhagen, C. J. Pickard, and S. Hamel, Phase behaviours of superionic water at planetary conditions, Nat. Phys. **17**, 1228 (2021).

[16] V. B. Prakapenka, N. Holtgrewe, S. S. Lobanov, and A. F. Goncharov, Structure and properties of two superionic ice phases, Nat. Phys. **17**, 1233 (2021).

[17] S. Sun, Y. He, D. Y. Kim, and H. Li, Anomalous elastic properties of superionic ice, Phys. Rev. B **102**, 104108 (2020).
[18] F. Matusalem, J. S. Rego, and M. de Koning, Plastic deformation of superionic water ices, Proc. Natl Acad. Sci. USA **119**, e2203397119 (2022).
[19] F. Grasselli, L. Stixrude, and S. Baroni, Heat and charge transport in H_2O at ice-giant conditions from ab initio molecular dynamics simulations, Nat. Commun. **11**, 3605 (2020).
[20] J. A. Thomas, J. E. Turney, R. M. Iutzi, C. H. Amon, and A. J. H. McGaughey, Predicting phonon dispersion relations and lifetimes from the spectral energy density, Phys. Rev. B **81**, 081411(R) (2010).
[21] See Supplemental Material at http://link.aps.org/supplemental/10.1103/m1s6-6hdf for calculation details, derivation of Born–von Kármán model, and additional figures, which also includes Refs. [37–43].
[22] Z. Fan, Z. Zeng, C. Zhang, Y. Wang, K. Song, H. Dong, Y. Chen, and T. Ala-Nissila, Neuroevolution machine learning potentials: Combining high accuracy and low cost in atomistic simulations and application to heat transport, Phys. Rev. B **104**, 104309 (2021).
[23] G. Kresse and J. Hafner, *Ab initio* molecular dynamics for liquid metals, Phys. Rev. B **47**, 558 (1993).
[24] J. Han, B. Xu, M. Hu, Y. H. Lin, and W. Liu, Analytical study on the size effect of phonon spectral energy density resolution, Comput. Mater. Sci. **132**, 6 (2017).
[25] A. G. Every, General closed-form expressions for acoustic waves in elastically anisotropic solids, Phys. Rev. B **22**, 1746 (1980).
[26] R. Caracas, Dynamical instabilities of ice X, Phys. Rev. Lett. **101**, 085502 (2008).
[27] A. Togo, L. Chaput, T. Tadano, and I. Tanaka, Implementation strategies in phonopy and phono3py, J. Phys. Condens. Matter **35**, 353001 (2023).
[28] G. Radtke, S. Klotz, M. Lazzeri, P. Loubeyre, M. Krisch, and A. Bossak, Phonon dispersion and proton disorder of ice VII and VIII, Phys. Rev. Lett. **132**, 056102 (2024).
[29] R. Qiu, Q. Zeng, H. Wang, D. Kang, X. Yu, and J. Dai, Anomalous thermal transport across the superionic transition in ice, Chin. Phys. Lett. **40**, 116301 (2023).
[30] W. Petry, A. Heiming, J. Trampenau, M. Alba, C. Herzig, H. R. Schober, and G. Vogl, Phonon dispersion of the bcc phase of group-IV metals. I. bcc titanium, Phys. Rev. B **43**, 10933 (1991).
[31] D. de Fontaine, N. E. Paton, and J. C. Williams, The omega phase transformation in titanium alloys as an example of displacement controlled reactions, Acta Metall. **19**, 1153 (1971).
[32] L. Sandoval, H. M. Urbassek, and P. Entel, The Bain versus Nishiyama–Wassermann path in the martensitic transformation of Fe, New J. Phys. **11**, 103027 (2009).
[33] Y. Takii, K. Koga, and H. Tanaka, A plastic phase of water from computer simulation, J. Chem. Phys. **128**, 204501 (2008).
[34] M. Rescigno, A. Toffano, U. Ranieri, L. Andriambariarijaona, R. Gaal, S. Klotz, M. M. Koza, J. Ollivier, F. Martelli, J. Russo, F. Sciortino, J. Teixeira, and L. E. Bove, Observation of plastic ice VII by quasi-elastic neutron scattering, Nature (London) **640**, 662 (2025).
[35] L. Wang, B. Liu, H. Li, W. Yang, Y. Ding, S. V. Sinogeikin, Y. Meng, Z. Liu, X. C. Zeng, and W. L. Mao, Long-range ordered carbon clusters: A crystalline material with amorphous building blocks, Science **337**, 825 (2012).
[36] H. Ding *et al.*, GitHub, 2026, https://github.com/Ding-Hairui/Phonon_SED.
[37] J. M. Dickey and A. Paskin, Computer simulation of the lattice dynamics of solids, Phys. Rev. **188**, 1407 (1969).
[38] L. T. Kong, Phonon dispersion measured directly from molecular dynamics simulations, Comput. Phys. Commun. **182**, 2201 (2011).
[39] Z. Fan *et al.*, GPUMD: A package for constructing accurate machine-learned potentials and performing highly efficient atomistic simulations, J. Chem. Phys. **157**, 114801 (2022).
[40] M. T. Dove, *Introduction to Lattice Dynamics* (Cambridge University Press, Cambridge, 1993).
[41] K. Song *et al.*, General-purpose machine-learned potential for 16 elemental metals and their alloys, Nat. Commun. **15**, 10208 (2024).
[42] D. Frenkel and A. J. Ladd, New Monte Carlo method to compute the free energy of arbitrary solids. Application to the fcc and hcp phases of hard spheres, J. Chem. Phys. **81**, 3188 (1984).
[43] R. Freitas, M. Asta, and M. de Koning, Nonequilibrium free-energy calculation of solids using LAMMPS, Comput. Mater. Sci. **112**, 333 (2016).